A New Soft-Switched Contactless Battery Charger with Robust Local Controllers

Yungtaek Jang and Milan M. Jovanović
DELTA Products Corporation
Power Electronics Laboratory
P.O. Box 12173, 5101 Davis Drive
Research Triangle Park, NC 27709, USA

Abstract - **A new soft-switched contactless battery charger with an improved local controller is described. The controller consists of a primary-current feedback control circuit in the inverter side and an output-voltage feedback control circuit in the rectifier side. By controlling the primary current of the inverter side, the maximum transferable power through the inductive coupling is automatically kept constant over the entire input voltage and load ranges. As a result, excessive circulating energy in the charger is minimized. Moreover, by incorporating the proposed controller, zero-voltage switching (ZVS) of all power switches is achieved. Finally, the proposed controller provides a tight regulation of the output voltage over the entire load and input voltage ranges without any feedback connection between the rectifier side and the inverter side.**

1. Introduction

Transmitting electric power through an inductive coupling is a good scheme for applications such as contactless battery chargers without direct electrical connections between a primary inverter and a secondary rectifier. Since the winding of the primary inverter and the winding of the secondary rectifier are inductively coupled through the air, electric power is transferred from the primary winding to the secondary winding in a magnetic energy form. Therefore, the contactless battery charger does not need any electrical contact [1] – [5]. However, it should be noted that a power transmission using an inductive coupling has several problems achieving high efficiency and supplying well-regulated output voltage as indicated in [2] and [4].

Because of the separated primary and secondary windings, a leakage inductance in an inductive coupling is not negligible when it is compared to a conventional transformer with well interleaved windings. Therefore, the energy stored in a leakage inductance causes high parasitic ringing and loss of energy.

Also, regulation of power transmission from the primary inverter to the secondary rectifier is difficult without an extra feedback connection that transfers output voltage information from the rectifier to the inverter.

Recently, a hard-switched contactless battery charger (shown in Fig. 1) using an input-voltage feedforward control for the inverter side and a pulse-width-modulator (PWM) output-voltage feedback control for the rectifier side has been introduced [6]. As shown in Fig. 1, the inverter side and the rectifier side have independent local controls to regulate the output voltage without any feedback connection between the rectifier side and the inverter side. Moreover, the contactless battery charger in Fig. 1 utilizes the energy stored in the leakage inductances of the transformer since the power stage incorporates the leakage inductances in the operation of the circuit.

However, the input voltage feedforward controller, as shown in Fig. 1, cannot automatically adjust the switching frequency with respect to a load variation, i.e., the maximum transferable power through the inductive coupling is not constant over the entire load range. As a result, it causes extra circulating energy and conduction losses at a light load. Moreover, as shown in Fig. 1, a ramp signal for PWM in the rectifier side is proportional to the sine-wave voltage waveform induced across the secondary resonant capacitor. Therefore, the PWM gain in the controller varies with respect to the load, i.e., the ratio of the duty cycle variation to the output voltage variation is much larger at full load than it is at light load. As a result, the compensator circuit of the output voltage feedback control becomes complex in order to guarantee reliable operation over the entire load range.

Finally, switch S_S of the controlled rectifier in Fig. 1 turns

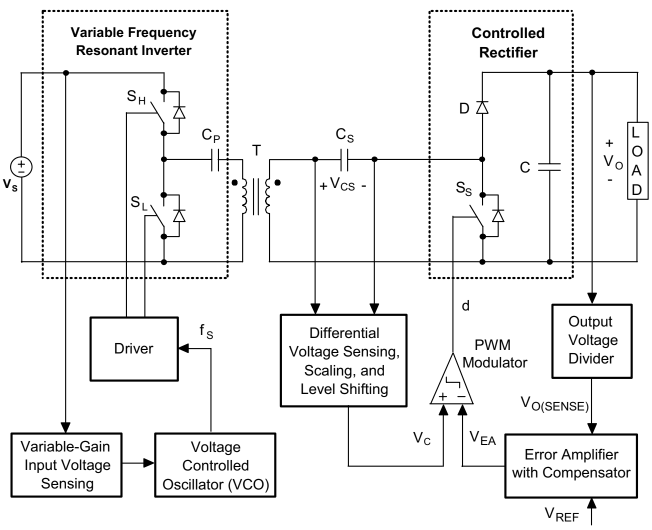

Fig. 1. Block diagram of conventional battery charger in [6].

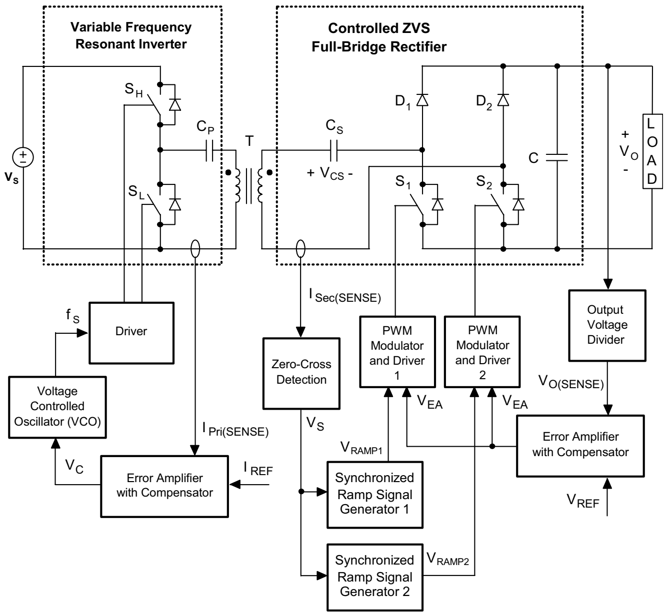

Fig. 2. Block diagram of proposed inductive battery charger with robust controller.

on by hard switching, i.e., switch S_S turns on when the voltage across the switch is equal to the output voltage. Hard switching of a power switch is not desirable because it increases conductive noise and the total loss in the contactless battery charger.

In this paper, a new soft-switched contactless battery charger with improved local controllers that is suitable for an efficient operation is described. As shown in Fig. 2, the proposed control scheme consists of a primary-current feedback control circuit in the inverter side and an output-voltage feedback control circuit in the rectifier side. The high efficiency of the contactless battery charger is achieved by using the proposed controller which eliminates excessive circulating energy and related conduction losses. The switching frequency in the inverter is controlled to keep the magnitude of the primary current constant over the entire input voltage and load ranges, so that the maximum transferable power through the inductive coupling is automatically kept constant without excessive circulating energy.

By incorporating the proposed controller to the contactless battery charger, not only do the switches in the inverter side achieve zero-voltage switching (ZVS), but also the switches in the rectifier side, too. Moreover, the reliable operation of a contactless battery charger over an entire load range is achieved by using robust ramp signals that provide the output voltage feedback controller with a constant PWM gain. The proposed controller also provides a tight regulation of output voltage over the entire load and input ranges without any feedback connection between the rectifier side and the inverter side.

The performance of the proposed soft-switched contactless charger with the improved controller was evaluated on a 36-W, universal-line-range prototype circuit operating over a switching frequency range from 124 kHz to 328 kHz. The measured efficiencies are approximately 84.4% at full load and minimum input voltage and approximately 78.5% at full load and maximum input voltage.

2. Analysis of Operation

A block diagram of the proposed battery charger is shown in Fig. 2. The system consists of a variable frequency resonant inverter on the input side and a controlled rectifier on the output side. They are inductively coupled through the transformer. The resonant current flowing through the primary winding of the transformer is sensed. The sensed current is used to control the switching frequency of the inverter so that the power transferred through the transformer is automatically maintained constant with the input voltage and load changes. As long as the switching frequency range is designed to be higher than the resonant frequency of the series resonant inverter, the switches of the inverter operates with ZVS and the switching frequency monotonically changes over the input voltage range. The bi-directional rectifier on the output side is controlled by a ZVS PWM control to maintain a tight regulation of the output voltage in the presence of a varying load.

Figure 2 shows a power stage of the contactless battery charger with a series resonant inverter. The input power circuit consists of a pair of switches S_H and S_L and resonant capacitor C_P. The output rectifier circuit consists of secondary switches S_1 and S_2, resonant capacitor C_S, diodes D_1 and D_2, and filter capacitor C. The switches are shown with their antiparallel diodes. To facilitate the analysis of the circuit, Fig. 3 shows the circuit in Fig. 2 with leakage inductance L_P, L_S, and magnetizing inductance L_M of the transformer. To simplify the analysis of operation, it is assumed that the input- and output-ripple voltages are negligible so that the voltages across the input and output

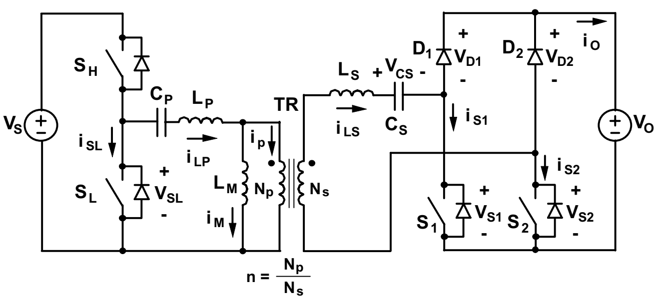

Fig. 3. Simplified schematic diagram of the power stage that shows leakage and magnetizing inductances of the transformer and reference directions of current and voltages.

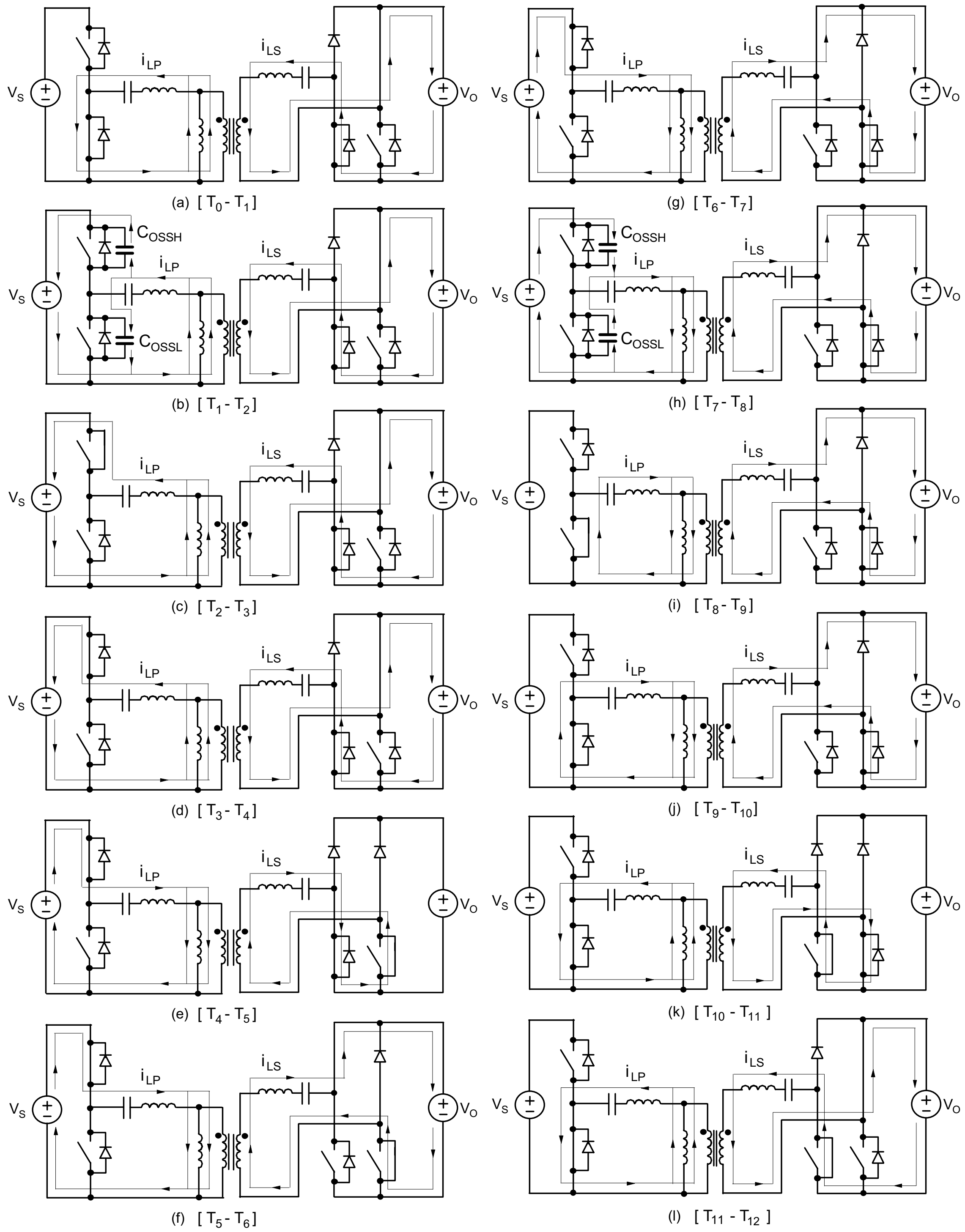

Fig. 4. Topological stages of the proposed inductive battery charger.

filter capacitors can be represented by constant-voltage sources V_S and V_O, respectively.

To further facilitate the explanation of the operation, Fig. 4 shows topological stages of the circuit in Fig. 3 during a switching cycle, whereas Fig. 5 shows the power-stage key waveforms for operation above the resonant frequency.

To further simplify the analysis, the following analysis of operation assumes that all semiconductor components in the circuit are ideal. i.e., that they exhibit zero resistance when in the on state and infinite resistance in the off state. Moreover, the magnetizing current i_M in Fig. 3 is in phase with resonant current i_{LS}. Nevertheless, these assumptions do not have any significant effect on the explanation of the principle of operation for the proposed circuit.

Before secondary switch S_1 is turned on at $t=T_0$, negative primary side resonant current $i_{LP}=i_M+i_P=i_M+i_{LS}/n$ flows through leakage inductance L_P, resonant capacitor C_P, and low-side switch S_L, whereas negative secondary-side resonant current i_{LS} flows through leakage inductance L_S, resonant capacitor C_S, output diode D_2, and the antiparallel diode of secondary switch S_1, as shown in Fig. 4(l). At the same time, output diode D_1 and secondary switch S_2 are off blocking output voltage V_0, whereas, high-side switch S_H is off blocking input voltage V_S. As a result, secondary switch S_1 turns on with ZVS at $t=T_0$, as shown in Fig. 4(a).

After secondary switch S_1 is turned on, the direction of the resonant current is not changed until low-side switch S_L is turned off at $t=T_1$. After low-side switch S_L is turned off at $t=T_1$, resonant current i_{LP}, which is flowing through switch S_L, is diverted from the switch to its output capacitance

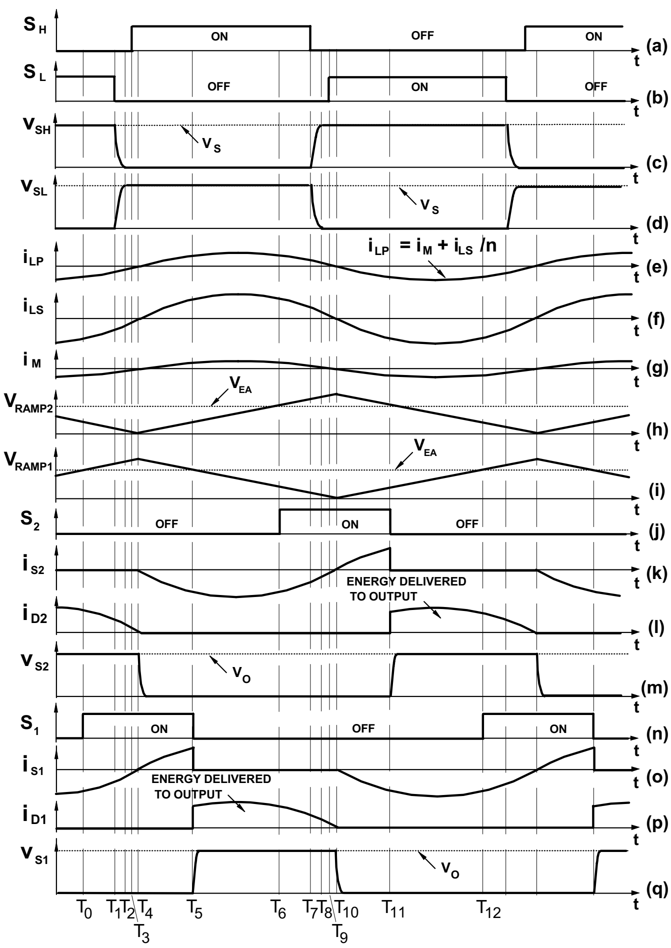

Fig. 5. Key waveforms of the proposed inductive battery charger.

C_{OSSL}, as shown in Fig. 4(b). As a result, the voltage across switch S_L starts increasing, whereas the voltage across high-side switch S_H starts decreasing, as illustrated in Figs. 5(c) and 5(d). This happens because the sum of the voltage across switches S_L and S_H is equal to input voltage V_S. When the voltage across high-side switch S_H reaches zero at $t=T_2$, i.e., when output capacitance C_{OSSH} of high-side switch S_H is fully discharged, the antiparallel diode of high-side switch S_H begins to conduct, as shown in Fig. 4(c). At the same time, low-side switch S_L is off, blocking input voltage V_S. After $t=T_2$, input voltage V_S is connected to the resonant circuit, which causes an increase in the resonant current. This topological stage ends at $t=T_4$, when i_{LP} reaches zero and the antiparallel diode of high-side switch S_H stops conducting. As can be seen from Fig. 5(e), to achieve ZVS of S_H, it is necessary to turn on S_H while its antiparallel diode is conducting. In Fig. 5, high-side switch S_H is turned on at $t=T_3$ with ZVS. As a result, after $t=T_4$, resonant current i_{LP} continues to flow through closed switch S_H, as shown in Fig. 4(e). Because of the assumption that currents i_M and i_{LS} are in phase with current i_{LP}, when the direction of current i_{LP} is reversed at $t=T_4$, the direction of i_M and i_{LS} is also reversed, as illustrated in Figs. 5(e)-5(g). Consequently, at $t=T_4$, current i_{LS}, which was flowing through output diode D_2 and the antiparallel diode of switch S_1, is diverted to the antiparallel diode of switch S_2 and switch S_1, as shown in Fig. 4(e). This topological stage ends at $t=T_5$, when secondary switch S_1 is turned off. After secondary switch S_1 is turned off at $t=T_5$, primary side resonant current i_{LP} flows through leakage inductance L_P, resonant capacitor C_P, and high-side switch S_H, whereas secondary-side resonant current i_{LS} flows through leakage inductance L_S, resonant capacitor C_S, output diode D_1, and the antiparallel diode of secondary switch S_2, as shown in Fig. 4(f). As a result, secondary switch S_2 can be turned on with ZVS at $t=T_6$, as shown in Fig. 4(g). This topological stage ends at $t=T_7$, when high-side switch S_H is turned off. After high-side switch S_H is turned off at $t=T_7$, resonant current i_{LP} flowing through switch S_H is diverted from the switch to its output capacitance C_{OSSH}, as shown in Fig. 4(h). As a result, output capacitance C_{OSSH} is being charged, whereas output capacitance C_{OSSL} is being discharged. When output capacitance C_{OSSL} is fully discharged at $t=T_8$, the antiparallel diode of low-side switch S_L begins to conduct, as shown in Fig. 4(i). At the same time, high-side switch S_H is off, blocking input voltage V_S. This topological stage ends at $t=T_{10}$, when i_{LP} reaches zero and the antiparallel diode of low-side switch S_L stops conducting. To achieve ZVS of S_L, it is necessary to turn on S_L while its antiparallel diode is conducting. In Fig. 5, low-side switch S_L is turned on at $t=T_9$ with ZVS. As a result, after $t=T_{10}$, resonant current i_{LP} continues to flow through closed switch S_L, as shown in Fig. 4(j). As shown in Figs. 4(k) and 5, after $t=T_{10}$, the direction of currents i_{LP}, i_M, and i_{LS} are reversed so that current i_{LP} flows through S_L, whereas current i_{LS} flows through switch S_2 and the antiparallel diode of switch S_1, as shown in Fig. 4(k). The circuit stays in this topological stage until the next switching cycle is initiated at $t=T_{12}$.

As can be seen from Fig. 5, the voltage stress of switches S_H and S_L is always limited to input voltage V_S, while the voltage stress of S_1, S_2, D_1, and D_2 are always limited to the output voltage V_O.

Implementation of the controller for the contactless battery charger system is also shown in Fig. 2. The inverter control in Fig. 2 is implemented by the sensing circuit of primary current I_{PRI} and an error amplifier with compensator circuit which generates error signal V_C from sensed primary current signal $I_{PRI(SENSE)}$ and reference current signal I_{REF}. By changing frequency f_S of the voltage controlled oscillator (VCO), the inverter maintains a constant primary current over the entire input voltage and load ranges. The primary switches operate with ZVS when switching frequency f_S is higher than the resonant frequency of the series resonant inverter shown in Fig. 2. Moreover, the primary switches are able to operate with zero current switching (ZCS) when switching frequency f_S is lower than the resonant frequency of the series resonant inverter.

The output voltage control in Fig. 2 is implemented with the two PWM modulators of the controlled ZVS full-bridge rectifier. In this control, sensed output voltage $V_{O(SENSE)}$ is compared with reference voltage V_{REF} at the input of the error amplifier. The generated error signal V_{EA} at the output of the error amplifier is compared with ramp signals V_{RAMP1} and V_{RAMP2}. Ramp signals V_{RAMP1} and V_{RAMP2} are synchronized to the zero crossing of the secondary resonant current and 180° out of phase as shown in Figs. 5(h) and 5(i). By the comparisons between error signal V_{EA} and ramp signals V_{RAMP1} and V_{RAMP2}, gate signals S1 and S2 are generated as shown in Figs. 5(j) and 5(n). It should be noted that the generated gate signals make switches S1 and S2 turn on when their antiparallel diodes are conducting. As a result, by the proposed controller, not only the switches in the inverter side but also the switches in the rectifier side achieve ZVS.

3. Experimental Results

The performance of the proposed soft-switched contactless charger with the improved controller was evaluated on a 36-W (12 V/ 3 A), universal-line-range (90 - 265 V_{AC}) prototype circuit operating over a switching frequency range from 124 kHz to 328 kHz.

Because the drain voltages of switches S_H and S_L are clamped to the input voltage, the peak voltage stress on switches S_H and S_L is approximately 380 V. The peak current stress on switches S_H and S_L, which occurs at full load and low line, is approximately 0.6 A. Therefore, an IRF840 MOSFET (V_{DSS} = 500 V, I_D = 8 A, R_{DS} = 0.85 Ω) from IR was used for each of the switches. Since the drain voltages of secondary switches S_1 and S_2 are clamped to the output voltage, the peak voltage stress on switches S_1 and S_2 is

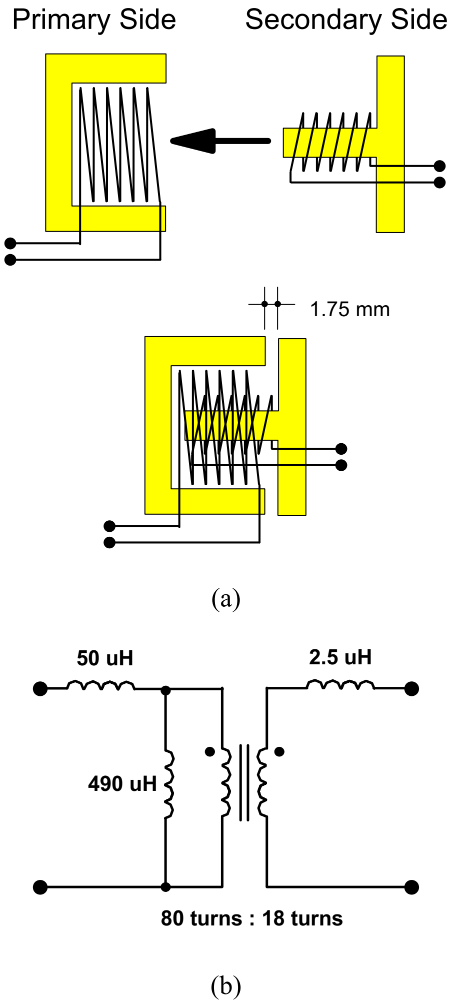

Fig. 6. (a) Winding structures and (b) equivalent circuit of inductive coupling transformer TR.

approximately 12 V. The peak current stress on switches S_1 and S_2 is approximately 3 A at full load. Therefore, a SI4810DY MOSFET (V_{DS} = 30 V, I_D = 10 A, R_{DS} = 0.0135 Ω) from VISHAY was used for each of the switches. This MOSFET has an embedded 4-A Schottky diode connected in parallel with its body diode.

Since output diodes D_1 and D_2 must block the output voltage and must conduct a half of the peak load current which is approximately 1.5 A, a MBR2045CT Schottky diode (V_{RRM} = 45 V, I_{FAVM} = 20 A) from On Semiconductor was used for each of output diodes D_1 and D_2. To reduce the conduction losses of the switches and output diodes, devices which have higher current ratings than the designed maximum current were selected.

A film capacitor (0.1 μF, 400 VDC) was used for primary resonant capacitor C_P. Two parallel connected film capacitors (1 μF, 100 VDC) were used for secondary resonant capacitor C_S.

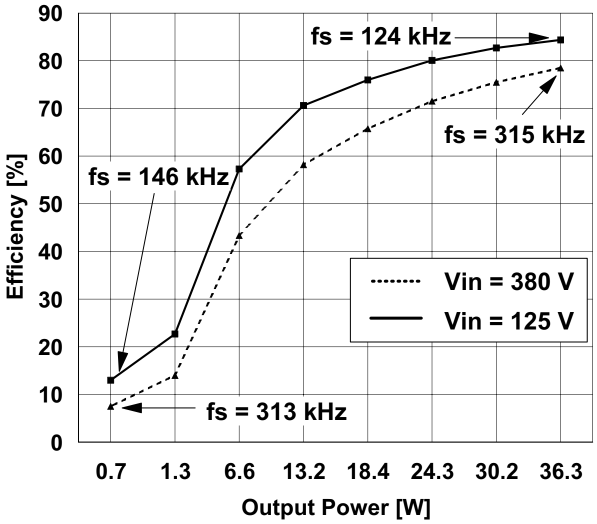

Fig. 7. Efficiency measurements of experimental circuit at output voltage $V_O = 12$ V.

As shown in Fig. 6, inductive coupling transformer TR was built using a pair of modified ferrite cores (EER28-3F3) with the primary winding (80 turns of AWG#44/75 strands Litz wire) and the secondary winding (18 turns of

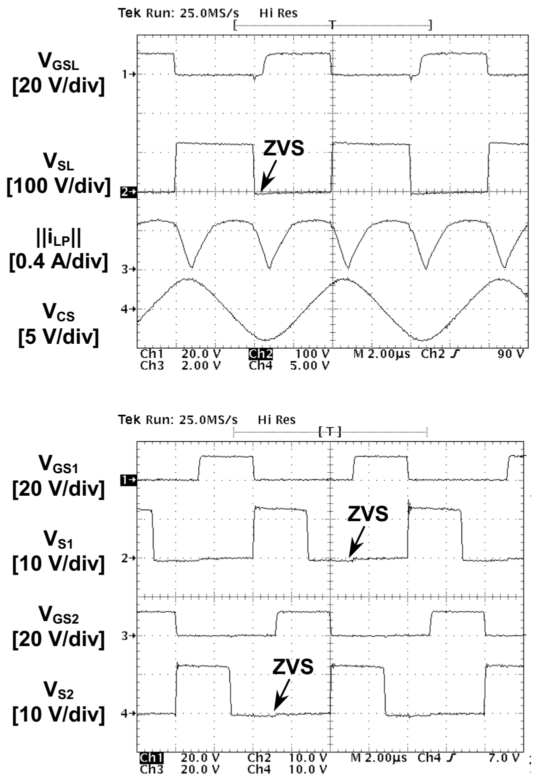

Fig. 8. Measured key waveforms of experimental circuit at V_{IN}=125 V, V_O=12 V, P_O=36 W. Time base: 2 μs/div.

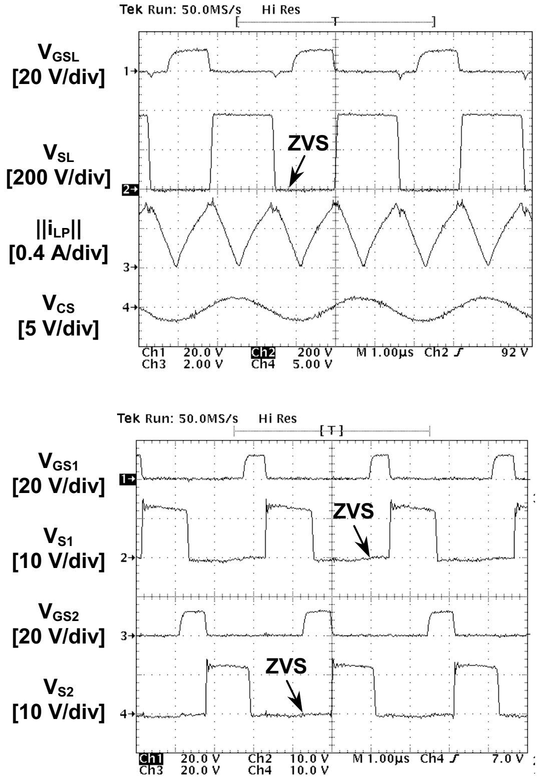

Fig. 9. Measured key waveforms of experimental circuit at V_{IN}=380 V, V_O=12 V, P_O=36 W. Time base: 1 μs/div.

AWG#42/150 strands Litz wire). As shown in Fig. 6(a), the middle leg and side legs of EER28-3F3 ferrite cores are removed to be used in the primary and secondary sides of inductive coupling transformer TR, respectively. The primary and secondary structures are separated by 1.75 mm distance.

The control circuit was implemented with controllers UC3863, LM319, AD817, and LM393. A TL431 voltage-reference IC is used to generate the output voltage reference for the locally controlled rectifier. An IR2110 driver is used to generate the required gate-drive signals for switches S_H and S_L. A TC427 driver is used to generate the required gate-drive signals for switches S_1 and S_2.

The output voltage of the experimental circuit is regulated well with a voltage ripple less than 2% over the entire input-voltage and load ranges. The measured efficiencies are approximately 84.4% at full load and minimum input voltage and approximately 78.5% at full load and maximum input voltage as shown in Fig. 7. Figures 8 and 9 show the oscillograms of key waveforms in the experimental circuit operating at full power from the low line and high line, respectively. As it can be seen from the corresponding waveforms in Fig. 5, there is a good agreement between the experimental and theoretical waveforms. As it can be seen from Figs. 5, 8, and 9, switches S_H, S_L, S_1, and S_2 are turned on with ZVS since their voltages fall to zero before gate-drive signals become high. Since all switches operate with ZVS, the contactless battery charger reduces switching losses and EMI problems.

4. Summary

A new soft-switched contactless battery charger with improved local controllers has been described. The analysis of its operation has been explained using topological stages and ideal waveforms. In the proposed circuit, by controlling the primary current of the inverter side, the maximum transferable power through the inductive coupling is kept constant over the entire input voltage and load ranges. As a result, excessive circulating energy in the charger is minimized. Moreover, zero-voltage switching of all the power switches is achieved. The proposed local controller on the secondary side provides a tight regulation of output voltage without any feedback connection between the rectifier side and the inverter side.

The performance of the proposed soft-switched contactless charger was evaluated on a 36-W, universal-line-range prototype circuit. The measured waveforms, which shows soft switching of all the switches, are provided to verify the analysis of operation and ideal waveforms. There is a good agreement between the experimental and theoretical waveforms. The measured full load efficiencies are approximately 84.4% and 78.5% at minimum and maximum input voltages, respectively.

References

[1] D.A.G. Pedder, A.D. Brown, and J.A. Skinner, "A Contactless Electrical Energy Transmission System,", *IEEE Trans. Industrial Electronics*, vol. 46, no. 1, pp. 23 – 30, Feb. 1999

[2] A. Ghahary and B.H. Cho, "Design of Transcutaneous Energy Transmission System Using a Series Resonant Converter," *IEEE Power Electronics Specialist's Conf. Record*, 1990, pp. 1 – 8.

[3] E. Dahl, *Induction Charging System,* U.S. Pat. 3,938,018, Feb. 10, 1976.

[4] C. G. Kim, D. H. Seo, J. S. You, J. H. Park, and B.H. Cho, "Design of a Contactless Battery Charger for Cellular Phone," *IEEE APEC Record*, 2000, pp. 769 – 773.

[5] Y. Kanai, M. Mino, T. Sakai, and T. Yachi, "A Non-Contact Power-Supply Card Powered by Solar Cells for Mobile Communications," *IEEE APEC Record*, 2000, pp. 1157 – 1162.

[6] Y. Jang and M. M. Jovanović, "A Contactless Electrical Energy Transmission System for Portable-Telephone Battery Chargers," *IEEE INTELEC Record*, 2000, pp. 726 – 732.